Complicated rupture process of the Mw 7.0 intraslab strike-slip earthquake in the Tohoku region on 10 July 2011 revealed by near-field pressure records

Tatsuya Kubota[1], Ryota Hino[1], Daisuke Inazu[2], Yoshihiro Ito[3], Takeshi Iinuma[4]

[1] Graduate School of Science, Tohoku University, Sendai, Japan.

[2] UTokyo Ocean Alliance, The University of Tokyo, Tokyo, Japan.

[3] Disaster Prevention Research Institute, Kyoto University, Uji, Japan.

[4] Japan Agency for Marine-Earth Science and Technology, Yokohama, Japan.

Corresponding Author: Tatsuya Kubota, Graduate School of Science, Tohoku University, 6-6, Aza-Aoba, Aramaki, Aoba-ku, Sendai 980-8578, Japan. (tatsuya.kubota.r6@dc.tohoku.ac.jp)

Key Points

An intraslab Tohoku strike-slip earthquake on July 2011 was studied with near-field pressure data

Two orthogonal faults related to the down-dip extensional stress were involved during the rupture

Estimated stress change around the rupture area was smaller than that in the outer-rise region

Abstract

We examined fault models of the Tohoku strike-slip intraslab earthquake (Mw 7.0) on 10 July 2011 using near-field tsunami data. After constraining the strike and location of the fault from tsunami source distribution, we investigated fault models assuming simple rupture of one fault, and simultaneous rupture of two conjugate faults. The estimated single fault reached >30 km down into the slab from the plate interface, suggesting bending stress enhancement after the 2011 Tohoku-Oki earthquake, but the depth extent was inconsistent with the aftershock activity. The model involving conjugate faults extended ~20 km below the slab surface, and was more consistent with the aftershocks. We concluded that it is more plausible that this earthquake involved two conjugate strike-slip faults, and the enhancement of the down-dip extensional stress after Tohoku-Oki earthquake was not large enough to allow rupture to propagate deeply into the slab beneath the landward slope of the Japan Trench.

Index Terms

Primary: Dynamics and mechanics of faulting (8118)

1: Tsunamis and storm surges (4564)

2: Subduction zones (7240)

3: Stresses: crust and lithosphere (8164)

4: Fractures and faults (8010)

Keywords

1. Fault modeling
2. Strike-slip earthquake
3. Intraslab earthquake
4. The 2011 Tohoku-Oki earthquake
5. Tsunami

6.Stress state

1. Introduction

The 2011 Mw 9.0 Tohoku-Oki earthquake ruptured a length of about 500 km along the Japan Trench [e.g., *Ide et al.*, 2011; *Ozawa et al.*, 2011; *Iinuma et al.*, 2012]. After this earthquake, many shallow (< ~20 km) normal-faulting aftershocks occurred in the up-dip portion of the subducting slab along the Japan Trench, activated by a tensional stress change associated with the Tohoku-Oki earthquake [e.g., *Asano et al.*, 2011; *Hasegawa et al.*, 2012; *Suzuki et al.*, 2012]. Before the 2011 Tohoku-Oki earthquake, the down-dip tensile stress field beneath the surface of the Pacific Plate near the trench and in the outer-rise region was estimated to flip to the down-dip compression field ~15 km below the slab surface [*Gamage et al.*, 2009; *Koga et al.*, 2012] (Figure 1). After the Tohoku-Oki earthquake, the stress regime at the depth of around 40 km in the outer-rise region changed from compression to tension [*Obana et al.*, 2012]. At the deep edge of the large coseismic slip area of the mainshock, *Ohta et al.* [2011] suggested that the stress-neutral plane of the double-plane deep seismic zone [*Hasegawa et al.*, 1978] was deepened by the stress change related to the Tohoku-Oki earthquake, based on the result of the coseismic fault model of the April 2011 Fukushima earthquake (M 7.1). However, the post-Tohoku-Oki-earthquake stress state beneath the plate surface in the inner trench area, especially around the extremely large (>50 m) coseismic slip area of the 2011 Tohoku-Oki earthquake, is still unclear.

On 10 July 2011, an Mw 7.0 intraslab earthquake with a focal depth of 17.5 km occurred ~50 km east of the epicenter of the Tohoku-Oki earthquake, close to the large coseismic slip area. The earthquake had a strike-slip focal mechanism with the T-axis in the down-dip direction (Global CMT, http://www.globalcmt.org) (Table 1). Since it is expected that this earthquake was induced by the stress enhancement of down-dip extension associated with the Tohoku-Oki earthquake, the intraslab stress state should be well represented in its rupture process. *Obana et al.* [2013] determined the location of the aftershocks of this strike-slip earthquake using the records of ocean bottom seismometers (OBSs), and found that the aftershock distribution formed two orthogonal lineations. The strikes of the lineations correspond to those of the two nodal planes of the focal mechanism, and it is suggested that two conjugate faults could be involved in the Mw 7.0 earthquake and its aftershock sequence. However, most of the relocated aftershock hypocenters were concentrated along the slab surface, so it is difficult to estimate the depth extent of the ruptured faults. Therefore, the finite source model of the M 7 strike-slip earthquake should provide important constraints on the post-2011 stress state, if it can be estimated.

When this event occurred, six ocean bottom pressure recorders (OBPRs) were deployed near the epicenter, and they observed a tsunami and static seafloor vertical deformation (Figures 1 and 2). The use of such near-field OBPR data will be helpful to estimate the source models and reveal the source processes of the offshore earthquakes, which are difficult to investigate using only onshore data (e.g., GPS, seismometers, strainmeters). For instance, *Saito et al.* [2010] demonstrated that high-quality tsunami waveform records obtained at offshore stations could help to resolve the detailed picture of the fault model for the 2004 off the Kii Peninsula earthquake (Mw 7.4). The purposes of this study are to estimate the source model of the 2011 Mw 7.0 intraslab event using near-field OBPR data and to discuss the stress state beneath the plate surface in the inner trench area.

2. Data

The OBPRs, which measure high-frequency quartz oscillations associated with both pressure and temperature, are identical to those used in the study of the crustal deformation associated with the Tohoku-Oki earthquake [*Hino et al.*, 2014]. The recorded oscillation frequencies of quartz sensors were converted to absolute pressure on the seafloor [e.g., *Matsumoto et al.*, 2012] and 1-s averages of them were taken.

From the pressure records, we estimated and removed ocean tide components using the tidal analysis program BAYTAP-G [*Tamura et al.,* 1991]. Then, we applied a digital recursive low-pass filter [*Saito*, 1978] to reduce high-frequency fluctuations associated with the seismic and hydroacoustic waves of large amplitudes. The optimum filter cutoff frequency was determined by minimizing the filtering effect on the tsunami signals and by suppressing the high-frequency components sufficiently (Figure S1). We adopted 10 mHz as an appropriate cutoff frequency for the present OBPR waveforms. The maximum amplitudes of the tsunami reached about 7 cm, and static seafloor vertical deformation of about 3 cm was also recorded at the nearest (~30 km) station, GJT3 (Figure 2). The travel time of the tsunami was less than 15 min for all the stations, and the duration times of the main tsunami pulses were about 4 min.

3. Tsunami Waveform Inversion

We first estimated the initial sea-surface height distribution by applying tsunami waveform inversion, because the geometry of the source fault is unclear based on only the seismic wave analysis of inland stations. The tsunami Green's functions were calculated by solving the linear dispersive tsunami equation using a finite difference approximation in local Cartesian coordinates [e.g., *Saito et al.*, 2010; *Saito et al.*, 2014]. In the calculation, the water height anomaly was transformed to bottom pressure, assuming that 1 cm of water height is equivalent to 1 hPa of bottom pressure. The spatial grid interval and time step interval of the calculation were 2 km and 1 s, respectively. As the bathymetry data, we interpolated ETOPO1 [*Amante and Eakins*, 2009]. The rupture duration *T* was assumed to be 0 s. The static offsets in the pressure records related to the vertical seafloor deformation were corrected using the method proposed by *Tsushima et al*. [2012]. In this study, we distributed pyramid-like-shaped unit sources of the sea surface displacement with the size of 20 km × 20 km in the area 180 km in the EW direction and 170 km NS around the hypocenter (rectangular area shown in Figure 1). Each unit source is located with an interval of 10 km and overlaps with next ones (Text S1 and Figure S2). The same low-pass filter that was applied to the observed records was also applied to the Green's functions. In the inversion, we calculated waveform residuals in a time window of 20 minutes from the origin time (white back ground area in Figure 2). We applied a smoothing constraint in the inversion by adjusting its weight based on inspecting the trade-off relationship between the weight and RMS misfit (Figure S3).

The obtained initial sea surface height distribution is shown in Figure 1. The diameter of the major uplift zone was about 50 km, and the peak uplift and subsidence were 4.9 cm and 3.9 cm, respectively. The spatial pattern of the seafloor deformation was consistent with the focal mechanism estimated from seismological data. The locations and strikes of the hinge lines between the uplift/subsidence areas corresponded well to the aftershock lineations [*Obana et al.*, 2013]. Tsunami waveforms calculated from the model were in good agreement with the observation (Figure 2).

4. Fault Modeling with Grid-search Methods

We sought an optimum finite fault with uniform slip of the strike-slip earthquake using a grid-search method. We assumed that the location and strike of the fault were well constrained by the aftershock distribution, because of good consistency between the epicenter distribution and the initial sea surface height distribution inverted from the tsunami waveforms, as shown in the previous section. The strike angle is assumed to be 65°or 330° according to the nodal planes of the GCMT solution. Note that these directions match those of the aftershock lineations very well. The unknown parameters we searched for were the dip and rake angles, the locations of both ends of the fault along strike, and the depths of the top and bottom of the fault. The locations of these four ends of the fault were defined by distances from a reference point on the fault (Figure S4). We regarded a fault model with a strike of 65° (EW model) to be preferable because the mainshock hypocenter was located along the aftershock lineation with this strike. In the EW model, the hypocenter was used as the origin of the fault. However, we also tried to seek another model, assuming a fault with a strike of 330° (NS model), even though the hypocenter was not located on the aftershock lineation with this strike. In the analysis assuming the NS model, we set the reference point at the location of the GCMT centroid, since it is located near the intersection of the aftershock lineaments. The slip amount was adjusted so that the resultant seismic moment Mo is consistent with the Global CMT solution (3.96×10^{20} Nm) with a rigidity of 40 GPa.

The seafloor displacement field was calculated using *Okada's* [1992] equations, and converted to the initial sea surface displacement by applying the depth filter [*Saito and Furumura*, 2009]. In the depth filtering, we assumed a constant seafloor depth of 3.5 km, the average water depth in the source area. Tsunami waveforms were calculated by superposition of the Green's functions prepared for the inversion for the initial sea surface height. The search range of the grid-search is shown in Table S1. The results are shown in Table 1 and Figures 3 and S5.

We inspected the top 100 solutions in terms of the variance reduction of the waveform fit. Figures 3b, 3c, and 3d show the top 100 fault models projected onto the vertical cross section, and histograms of the model parameters. From these figures, it is clear that the dip and rake angles and the depth to the top of the fault (W2) are reasonably well constrained. Although the uncertainty of the depth of the bottom of the fault was large, the solutions with large fault widths tend to explain the observed data better. For example, the best-fit model with an EW fault plane is 30 km in width from the epicenter to the lower edge of the fault plane (W1) (Figure 3). However, the aftershocks are concentrated only in the shallowest part of the fault plane, and no aftershocks occur in the deeper part. Moreover, L/W ratios, ratios of the fault length (L = L2 – L1, Figure S4) to the width (W = W1 – W2, Figure S4) are less than one in most of the solutions (i.e., the fault width is greater than the length), as shown in Figure 3e. According to the empirical scaling relationship reported by *Wells and Coppersmith* [1994], a common M 7 class strike-slip earthquake has a fault width of ~15 km and an

L/W ratio of ~4. Our solution differs significantly from the standard picture, and a similar discrepancy is also seen in the NS fault model (Figure S5). Therefore, we conclude that the assumption of a single fault rupture caused this discrepancy.

5. Fault Modeling with Simultaneous Rupture of Conjugate Faults

One of the largest strike-slip intraplate earthquakes ever recorded, associated with a megathrust earthquake, was the 2012 Mw 8.6 Sumatra earthquake. The rupture occurred on the trench outer region of the source area of the 2004 Sumatra–Andaman earthquake (Mw 9.1). The earthquake had a complicated rupture process, which ruptured on distinct planes in an orthogonal fault system, based on seismic analyses [*Meng et al.*, 2012]. In a similar way, the Tohoku strike-slip earthquake may have ruptured two conjugate strike-slip faults in the subducting slab simultaneously. Here, we try to estimate a fault model consisting of two conjugate faults that ruptured simultaneously (hereafter, the conjugate model).

For simplicity in the modeling, Mo is divided equally between the two conjugate fault planes, and the search range for the fault length and location is mostly constrained based on the aftershock distribution, and the depths of the top and bottom of the two fault planes are required to be equal. We did not assume any time delay between the two subfaults, because the observed tsunami waveforms are composed of single large pulses, and it is unlikely that the tsunami data would have sufficient temporal resolution to distinguish the difference between the origin times of the ruptures of the two conjugate faults. Other settings are all the same as for the single fault model.

The fault parameters obtained from the conjugate model are shown in Table 1.

The initial sea surface displacement distribution expected from the conjugate model (Figure 4a) is similar to that from the single fault models (Figures 3 and S5) and resemble that obtained from direct inversion of the tsunami records (Figure 1). Tsunami waveforms synthesized from the conjugate model fit the observed ones well (Figure 2).

The depths of the bottom of the two fault planes were constrained to 15 km (Figures 4b, 4c, 4d), making the fault location more consistent with the aftershock distribution than the single fault models (red rectangles in Figure 3). The fault length appears to fall within the range of 10–30 km for the NE-SW fault and 20–30 km for the NW-SE fault, which are slightly shorter than the fault lengths expected for earthquakes of Mw 6.8 (equivalent to half of the total moment), ~40 km according to the scaling relationship of *Wells and Coppersmith* [1994]. The solutions tend to have an L/W ratio of ~1.4 (Figure 4e), which is greater than the majority of solutions with a single fault assumption, reducing the discrepancy with the empirical relationship.

We assumed here that the two conjugate faults to have equal amount of seismic moment, but that is not always the case. Since it required formidable computation time to seek a model by changing the moment ratio between the two faults, we only made the grid-searching with the ratio of 1:2 and 2:1 to assess the effect of the imbalance in the released moment. The best-fit model in the trial was that with the moment ratio of 2:1 between the EW and NS faults and its L/W ratio was similar to those of the best-fit single fault models (Figure S6). Since the single fault models can be regarded as the extreme case of the conjugate models with the moment ratio of 0:1 or 1:0, the result of the trial seems to be plausible. From this inspection, we conclude that the model with the conjugate fault of similar moment release amount is more consistent with aftershock distribution and with the empirical fault scaling relationship than any other models we sought so far.

6. Discussion and Conclusions

The focal mechanism of this earthquake was consistent with the pre-2011 down-dip extensional stress state in the shallow part of the subducting slab [e.g., *Gamage et al.*, 2009; *Obana et al.*, 2012], suggesting that the earthquake occurred in the tensional stress field near the slab surface enhanced by the Tohoku-Oki earthquake. Therefore, the depth extent of the coseismic rupture area is an important indicator of the post-Tohoku-Oki earthquake stress state in the subducting slab around the inner trench area.

Regardless of the strike, the single fault models derived from local tsunami waveform analysis extend deep into the slab, more than ~30 km below the plate interface. Before the Tohoku-Oki earthquake, the stress-neutral plane between the down-dip tensile field and the down-dip compression field near the surface of the slab was estimated to be ~15 km below the slab surface [*Gamage et al.*, 2009; *Koga et al.*, 2012]. After the Tohoku-Oki earthquake, *Obana et al.* [2012] reported that the down-dip extensional earthquakes occurred deeper than 30 km below the surface of the incoming plate, and suggested that the Tohoku-Oki earthquake made the tensile stress regime extend even deeper. If we assume a single fault rupture, we can interpret that the deep penetrations of the rupture plane of the single fault models suggest a manifestation of deepening of the lower limit of the extensional stress field in the inner trench area, as well as beneath the outer-rise region.

On the other hand, the coseismic rupture is not required to penetrate deep into the slab if we assume a conjugate fault model. The bottom of the fault was estimated to be ~20 km from the plate interface, which is reasonably consistent with the depth of the stress transition from shallow tensile to deep compressional intraslab stress before the Tohoku-Oki earthquake. Although it is difficult to determine which is better, the single or conjugate fault model, based only on the misfit of the tsunami waveforms, we concluded that the conjugate fault model is more probable because of its consistency with the depth distribution of the aftershocks. The disproportion of the lengths and widths of the single fault models is another reason we prefer the conjugate fault model. *Obana et al.* [2013] documented the fact that the conjugate aftershock lineations are related to the structural features within the Pacific slab [*Nakanishi et al.*, 1992]. If the strike-slip earthquake occurred as the reactivation of such pre-existing weak planes, their simultaneous rupture is probable. If conjugate rupture occurred during the earthquake, our result suggests that the enhancement of the down-dip tensile field associated with the 2011 Tohoku-Oki earthquake was not large enough to significantly deepen the extensional regime beneath the trench inner slope region, whereas remarkable change was found beneath the outer-rise region [*Obana et al.*, 2012].

Acknowledgements

The authors thank Dr. Tatsuhiko Saito of the National Research Institute for Earth Science and Disaster Prevention (NIED), for the Fortran code to calculate the tsunami, insightful discussions, and many helpful comments. Much support and advice of Dr. Yusaku Ohta of Tohoku University were so invaluable. This study was supported by the research project "Research concerning Interaction between the Tokai, Tonankai, and Nankai earthquakes" of the Ministry of Education, Culture, Sports, Science and Technology, and by JSPS KAKENHI (A) 20244070 and 26000002. The figures in this paper were prepared using Generic Mapping Tools (GMT) [*Wessel and Smith*, 1998]. The authors thank anonymous reviewers for constructive comments.

References

Amante, C., and B. W. Eakins (2009), ETOPO1 1 arc-minute global relief model: Procedures, data sources and analysis, in *NOAA Technical Memorandum NESDIS NGDC-24*, pp. 19.

Asano, Y., T. Saito, Y. Ito, K. Shiomi, H. Hirose, T. Matsumoto, S. Aoi, S. Hori, and S. Sekiguchi (2011), Spatial distribution and focal mechanisms of aftershocks of the 2011 off the Pacific coast of Tohoku Earthquake, *Earth Planets Space*, *63*, 669–673, doi: 10.5047/eps.2011.06.016.

Gamage, S. S. N., N. Umino, A. Hasegawa, and S. H. Kirby (2009), Offshore double-planed shallow seismic zone in the NE Japan forearc region revealed by sP depth phases recorded by regional networks, *Geophys. J. Int.*, *178(1)*, 195–214, doi: 10.1111/j.1365-246X.2009.04048.x.

Hasegawa, A., N. Umino, and A. Takagi (1978), Double-planed structure of the deep seismic zone in the northeastern Japan arc, *Tectonophysics, 47*, 43–58, doi:10.1016/0040-1951(78)90150-6..

Hasegawa, A., K. Yoshida, and T. Okada (2011), Nearly complete stress drop in the 2011 M_w 9.0 off the Pacific coast of Tohoku Earthquake, *Earth Planets Space*, *63*, 703–707, doi: 10.5047/eps.2011.06.007.

Hino, R., D. Inazu, Y. Ohta, Y. Ito, S. Suzuki, T. Iinuma, Y. Osada, M. Kido, H. Fujimoto, and Y. Kaneda (2014), Was the 2011 Tohoku-Oki earthquake preceded by aseismic preslip? Examination of seafloor vertical deformation data near the epicenter, *Mar. Geophys Res.*, *35*, 181–190, doi: 10.1007/s11001-013-9208-2.

Ide, S., A. Baltay, and G. C. Beroza (2011), Shallow dynamic overshoot and energetic deep rupture in the 2011 M_w 9.0 Tohoku-Oki earthquake, *Science*, *332*, 1426, doi:10.1126/science.1207020.

Iinuma, T., R. Hino, M. Kido, D. Inazu, Y. Osada, Y. Ito, M. Ohzono, H. Tsushima, S. Suzuki, H. Fujimoto, and S. Miura (2012), Coseismic slip distribution of the 2011 off the Pacific Coast of Tohoku Earthquake (M9.0) refined by means of seafloor geodetic data, *J. Geophys. Res.*, *117*, B07409, doi: 10.1029/2012JB009186.

Ito, A., G. Fujie, S. Miura, S. Kodaira, Y. Kaneda, and R. Hino (2005), Bending of the subducting oceanic plate and its implication for rupture propagation of large interplate earthquakes off Miyagi, Japan, in the Japan Trench subduction zone, *Geophys. Res. Lett.*, *32*, L05310, doi: 10.1029/2004GL022307.

Koga, S., Y. Ito, R. Hino, M. Shinohara, and N. Umino (2012), Focal mechanisms of small earthquakes within the Pacific plate near the Japan Trench, *Zisin* (2), *64*, 75–90, in Japanese with English abstract.

Matsumoto, H., S. Inoue, and T. Ohmachi (2012), Dynamic response of bottom water pressure due to the 2011 Tohoku earthquake, *J. Disaster Res.*, *7*(7), 468–475.

Meng, L., J. P. Ampuero, J. Stock, Z. Duputel, Y. Luo, and V. C. Tsai (2012), Earthquake in a maze: compressional rupture branching during the 2012 M_w 8.6 Sumatra earthquake, *Science*, *337*, 724–726, doi: 10.1126/science.1224030.

Nakanishi, M., K. Tamaki, and K. Kobayashi (1992), A new Mesozoic isochron chart of the northwestern Pacific Ocean: Paleomagnetic and tectonic implications, *Geophys. Res. Lett.*, *19*, 693–696.

Obana, K., G. Fujie, T. Takahashi, Y. Yamamoto, Y. Nakamura, S. Kodaira, N. Takahashi, Y. Kaneda, and M. Shinohara (2012), Normal-faulting earthquakes beneath the outer slope of the Japan Trench after the 2011 Tohoku earthquake: Implications for the stress regime in the incoming Pacific plate, *Geophys. Res. Lett.*, *39*, L00G24, doi: 10.1029/2011GL050399.

Obana, K., S. Kodaira, M. Shinohara, R. Hino, K. Uehira, H. Shiobara, K. Nakahigashi, T. Yamada, H. Sugioka, A. Ito, Y. Nakamura, S. Miura, T. No, and N. Takahashi (2013), Aftershocks near the updip end of the 2011 Tohoku-Oki earthquake, *Earth Planet. Sci. Lett.*, *382*, 111–116, doi: 10.1016/j.epsl.2013.09.007.

Ohta, Y., S. Miura, M. Ohzono, S. Kita, T. Iinuma, T. Demachi, K. Tachibana, T. Nakayama, S. Hirahara, S. Suzuki, T. Sato, N. Uchida, A. Hasegawa, and N. Umino, (2011), Large intraslab earthquake (2011 April 7, *M* 7.1) after the 2011 off the Pacific coast of Tohoku Earthquake (*M* 9.0): Coseismic fault model based on the dense GPS network data, *Earth Planets Space*, *63*, 1207–1211, doi: 10.5047/eps.2011.07.016.

Okada, Y. (1992), Internal deformation due to shear and tensile faults in a half-space, *Bull. Seismol. Soc. Am.*, *82*, 1018–1040.

Ozawa, S., T. Nishimura, H. Suito, T. Kobayashi, M. Tobita, and T. Imakiire (2011), Coseismic and postseismic slip of the 2011 magnitude-9 Tohoku-Oki earthquake, *Nature*, *475*, 373–376, doi: 10.1038/nature10227.

Saito, M. (1978), An automatic design algorithm for band selective recursive digital filters (in Japanese), *Butsuri Tanko*, *31*, 112–135.

Saito, T., and T. Furumura (2009), Three-dimensional tsunami generation simulation due to sea-bottom deformation and its interpretation based on the linear theory, *Geophys. J. Int.*, *178*, 877–888, doi: 10.1111/1365-246X.2009.04206.x.

Saito, T., K. Satake, and T. Furumura (2010), Tsunami waveform inversion including dispersive waves: the 2004 earthquake off Kii Peninsula, Japan, *J. Geophys. Res.*, *115*, B06303, doi: 10.1029/2009JB006884.

Saito, T., D. Inazu, T. Miyoshi, and R. Hino (2014), Dispersion and nonlinear effects in the 2011 Tohoku-Oki earthquake tsunami, *J. Geophys. Res.*, *119*, 5160–5180, doi: 10.1002/2014JC009971.

Suzuki, K., R. Hino, Y. Yamamoto, S. Suzuki, H. Fujimoto, M. Shinohara, M. Abe, Y. Kawaharada, Y. Hasegawa, and Y. Kaneda (2012), Seismicity near the hypocenter of the 2011 off the Pacific coast of Tohoku earthquake deduced by using ocean bottom seismographic data, *Earth Planets Space*, *64*, 1125–1135, doi: 10.5047/eps.2012.04.010.

Tamura, Y., T. Sato, M. Ooe, and M. Ishiguro (1991), A procedure for tidal analysis with a Bayesian information criterion, *Geophys. J. Int.*, *104*, 507–516, doi: 10.1111/j.1365-246X.1991.tb05697.x..

Tsushima, H., R. Hino, Y. Tanioka, F. Imamura, and H. Fujimoto (2012), Tsunami waveform inversion incorporating permanent seafloor deformation and its application to tsunami forecasting, *J. Geophys. Res.*, *117*, B03311, doi: 10.1029/2011JB008877.

Wells, D. L., and K. J. Coppersmith (1994), New empirical relationships among magnitude, rupture length, rupture width, rupture area, and surface displacement, *Bull. Seismol. Soc. Am.*, *84*(4), 974–1002.

Wessel, P., and W. Smith (1998), New, improved version of generic mapping tools released, *Eos Trans. AGU*, *79*(47), 579, doi: 10.1029/98EO00426.

Table 1. Comparison of fault parameters

Model	EW model	NS model	Conjugate model		Global CMT	
			EW fault	NS fault	EW fault	NS fault
Strike [°][a]	65	330	65	330	65	330
Dip [°]	85	80	90	85	74	75
Rake [°]	10	180	15	170	16	164
L1 [km]	- 5	- 5	- 10	- 10		
L2 [km]	0	10	10	15		
W1 [km]	- 30	- 30	- 15	- 15		
W2 [km]	0	0	0	0		
Slip amount [m]	6.6	2.2	1.7	1.3		
RMS misfit [cm]	0.603	0.679	0.615			

[a]Strike angle is fixed at Global CMT value.

Figure Captions

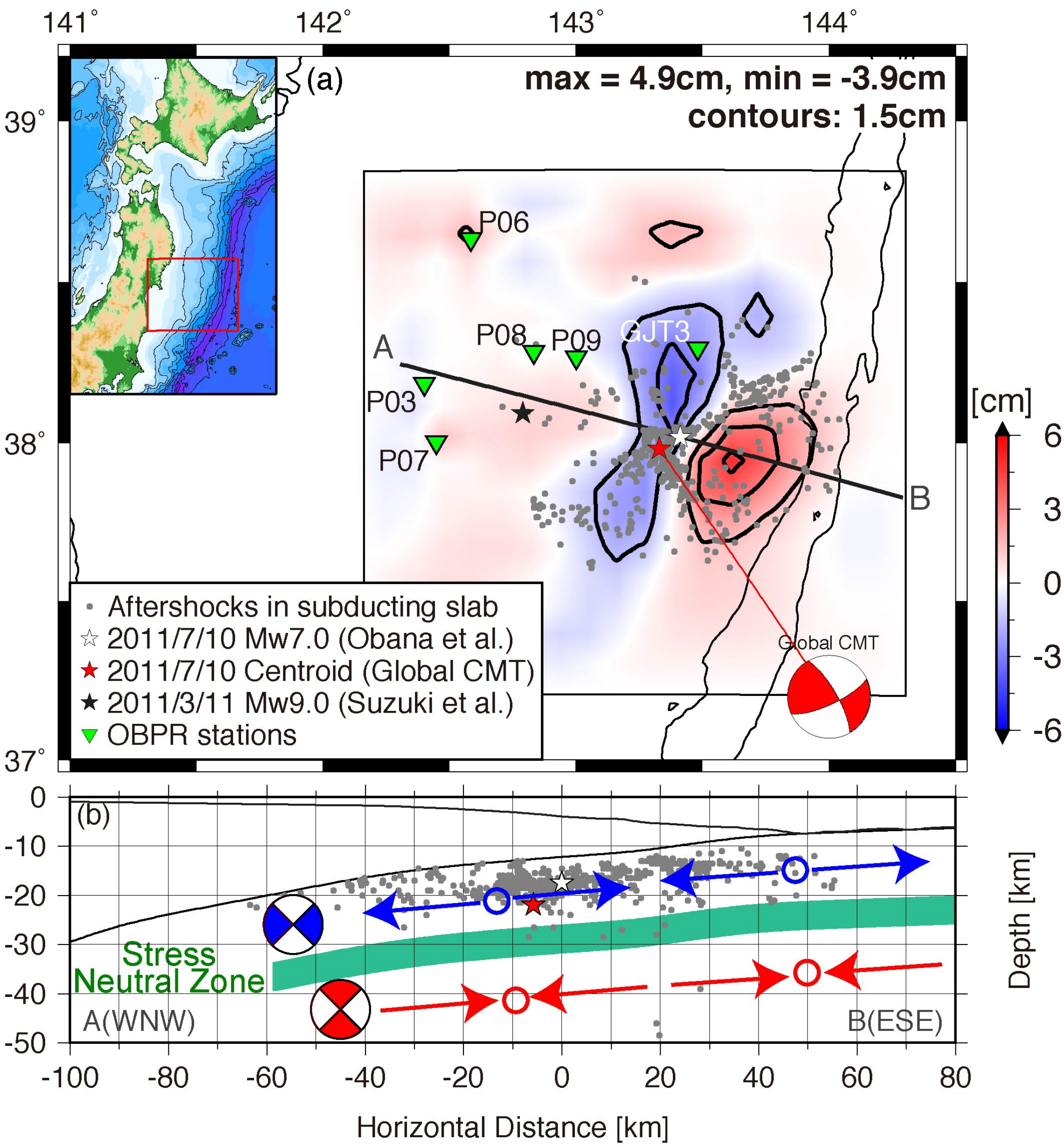

Figure 1. (a) Initial sea surface height distribution derived from tsunami waveform inversion. Black thin lines denote the analytical area. Uplift and subsidence areas are shown in red and blue, respectively. White and black stars are epicenters of Mw 7.0 event and Mw 9.0 mainshock, respectively. Contour interval is 1.5 cm. Small dots denote aftershocks. Red star and beach ball indicate focal mechanism. Green inverted triangles denote OBPR stations. (b) Vertical profile along A–B line in Figure 1a and

schematic illustration of the stress field before the 2011 Tohoku earthquake estimated by *Gamage et al.* [2009] and *Koga et al.* [2012]. The down-dip tensile stress field (blue allows and beach ball) flips to the down-dip compression field (red) ~15 km below the slab surface (shown by thick green line, stress neutral zone).

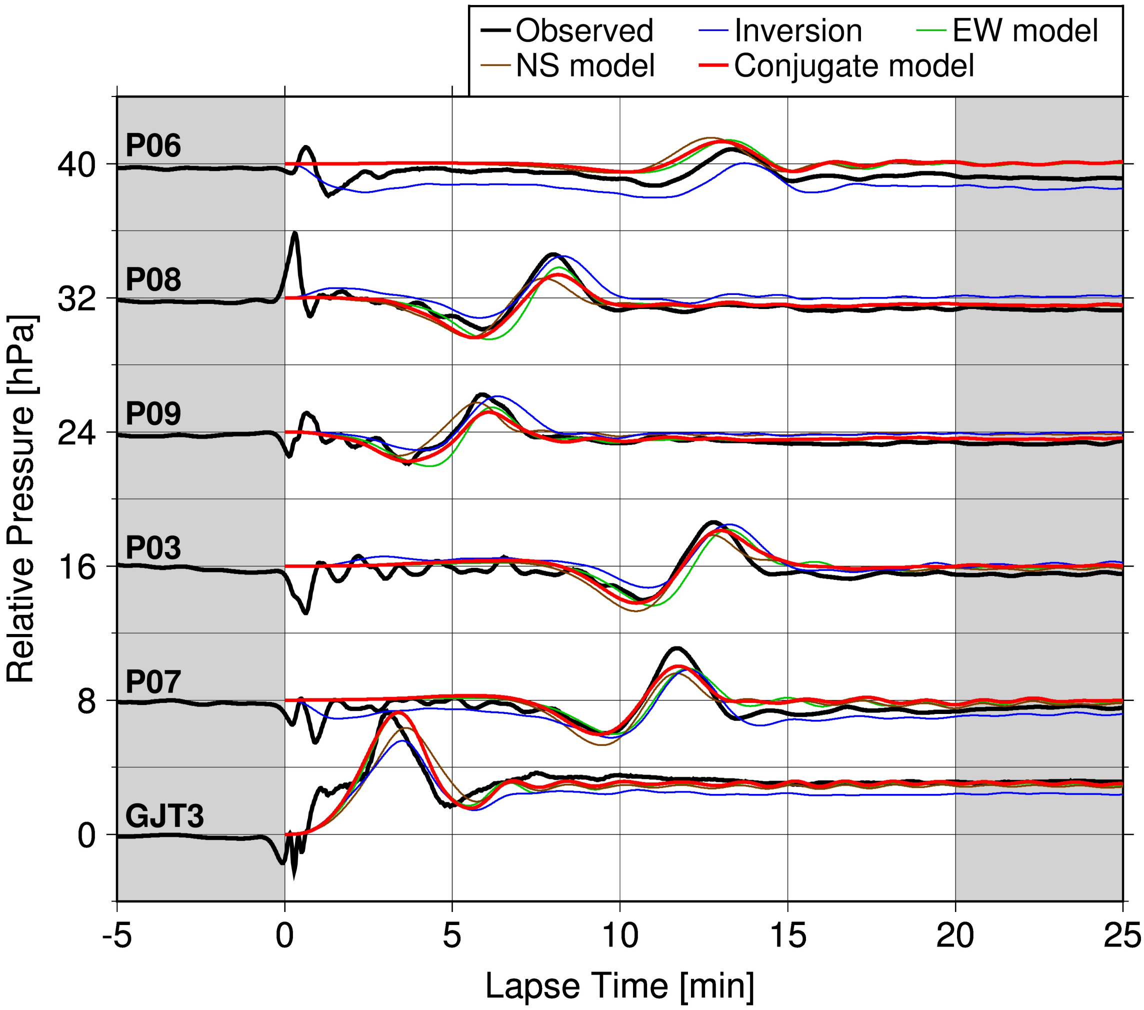

Figure 2. Comparisons between observed (black lines) and calculated waveforms derived from waveform inversion (blue), EW (green), NS (brown), and conjugate models (red).

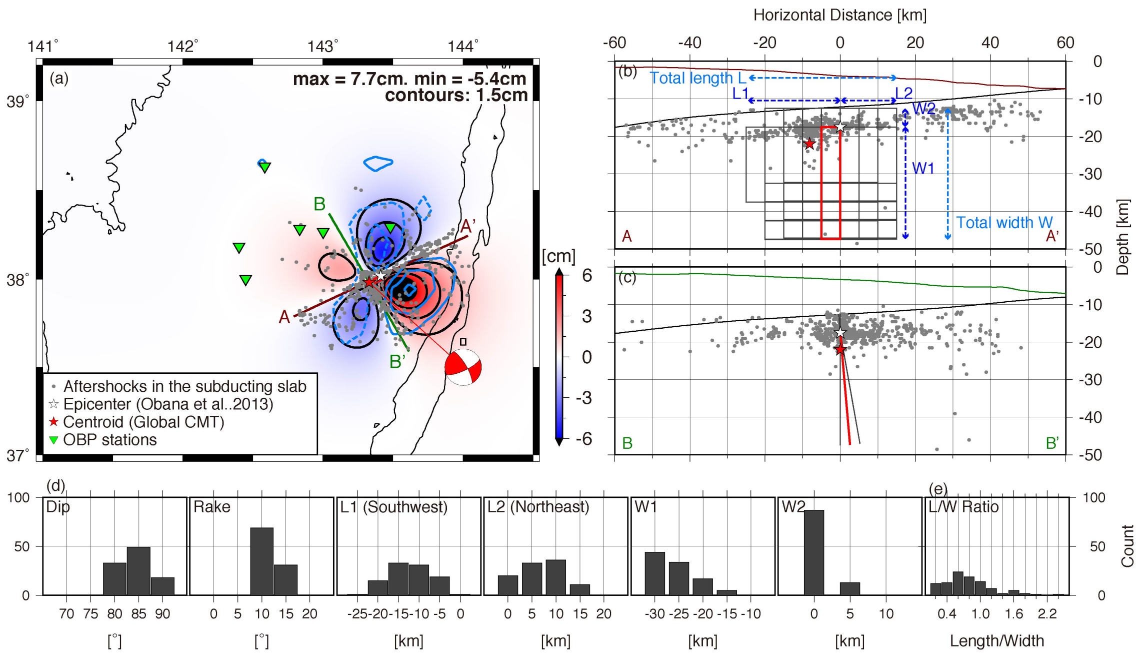

Figure 3. Grid-search results for EW model. (a) Initial sea surface height distribution derived from optimum fault model (black) and inversion (blue). (b) Vertical profile along A–A’ and (c) B–B’ line in Figure 3a. Red line denotes optimum fault. Black lines show top 100 solutions of grid search. Thick black curved line denotes plate boundary [*Ito et al.,* 2005]. (d) Histograms of model parameters. (e) Histogram of L/W ratios.

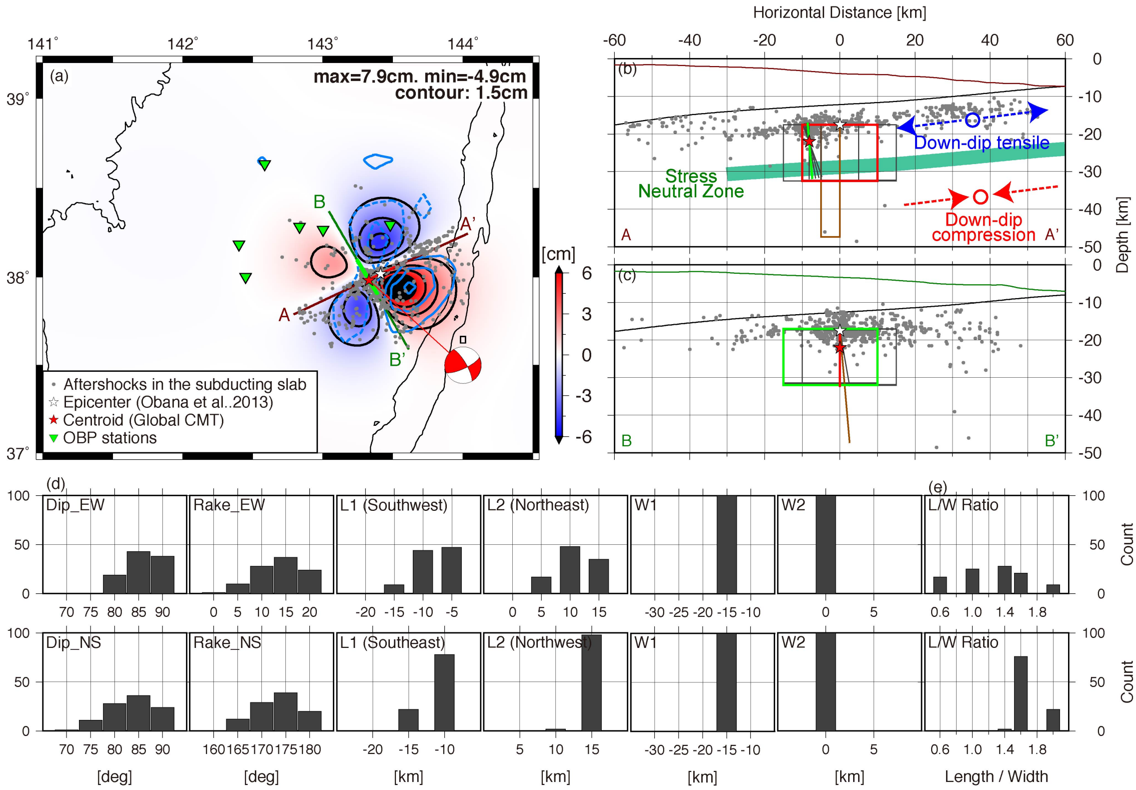

Figure 4. Grid-search results for conjugate model. (a) Initial sea surface height distribution derived from fault model (black) and inversion (blue). (b) Vertical profile of A–A' and (c) B–B' line in Figure 4a. Red and green lines denote optimum fault. Brown lines denote optimum EW model. Arrows indicate schematic image of stress field in shallower (blue) and deeper (red) portions of subducting slab, and the pre-2011 stress transition zone (thick green line) between them [*Koga et al.*, 2012]. (d) Histograms of model parameters. Upper and lower rows denote results of fault with strikes of 65° and 330°, respectively. (e) Histogram of L/W ratios.

Geophysical Research Letters

Supporting Information for

Complicated rupture process of the Mw 7.0 intraslab strike-slip earthquake in the Tohoku region on 10 July 2011 revealed by near-field pressure records

Tatsuya Kubota[1], Ryota Hino[1], Daisuke Inazu[2], Yoshihiro Ito[3], Takeshi Iinuma[4]

[1)] Graduate School of Science, Tohoku University, Sendai, Japan

[2)] UTokyo Ocean Alliance, The University of Tokyo, Tokyo, Japan

[3)] Disaster Prevention Research Institute, Kyoto University, Uji, Japan

[4)] I Japan Agency for Marine-Earth Science and Technology, Yokohama, Japan

Contents of this file

Introduction

Text S1 is the description of the assignment of the unit source used in the tsunami waveform inversion. Figure S1 shows the comparisons of the low-pass filtered waveform that was used to determine the optimum cutoff. A schematic illustration of assignment of the unit source used in the tsunami waveform inversion is shown in Figure S2. The trade-off relationship used to determine the smoothing weight in the tsunami source inversion is shown in Figure S3. A schematic of the unknown parameters in the grid search is shown in Figure S4. The result of the grid-search assuming a fault striking NW–SE (NS model) is shown in Figure S5. Figure S6 is the result of the grid-search assuming uneven Mo between two fault planes. Table S1 shows the search range for the unknown parameters in the grid-search analysis.

Text S1.

In the tsunami waveform calculation, we used the pyramid-like-shaped unit source expressed by the following form:

$$\eta_0(x,y) = \left(1 - \frac{|x-x_0|}{10}\right)\left(1 - \frac{|y-y_0|}{10}\right),$$
$$x_0 - 10 < x < x_0 + 10(km),$$
$$y_0 - 10 < y < y_0 + 10(km)$$

where $\eta_0(x, y)$ denotes the displacement of each unit source at the grid point (x, y) and (x_0, y_0) is the center of the unit source. The schematic illustration of the unit source is shown in Figure S3. Each unit source has the size of 20 km × 20 km, and is distributed with an interval of 10 km.

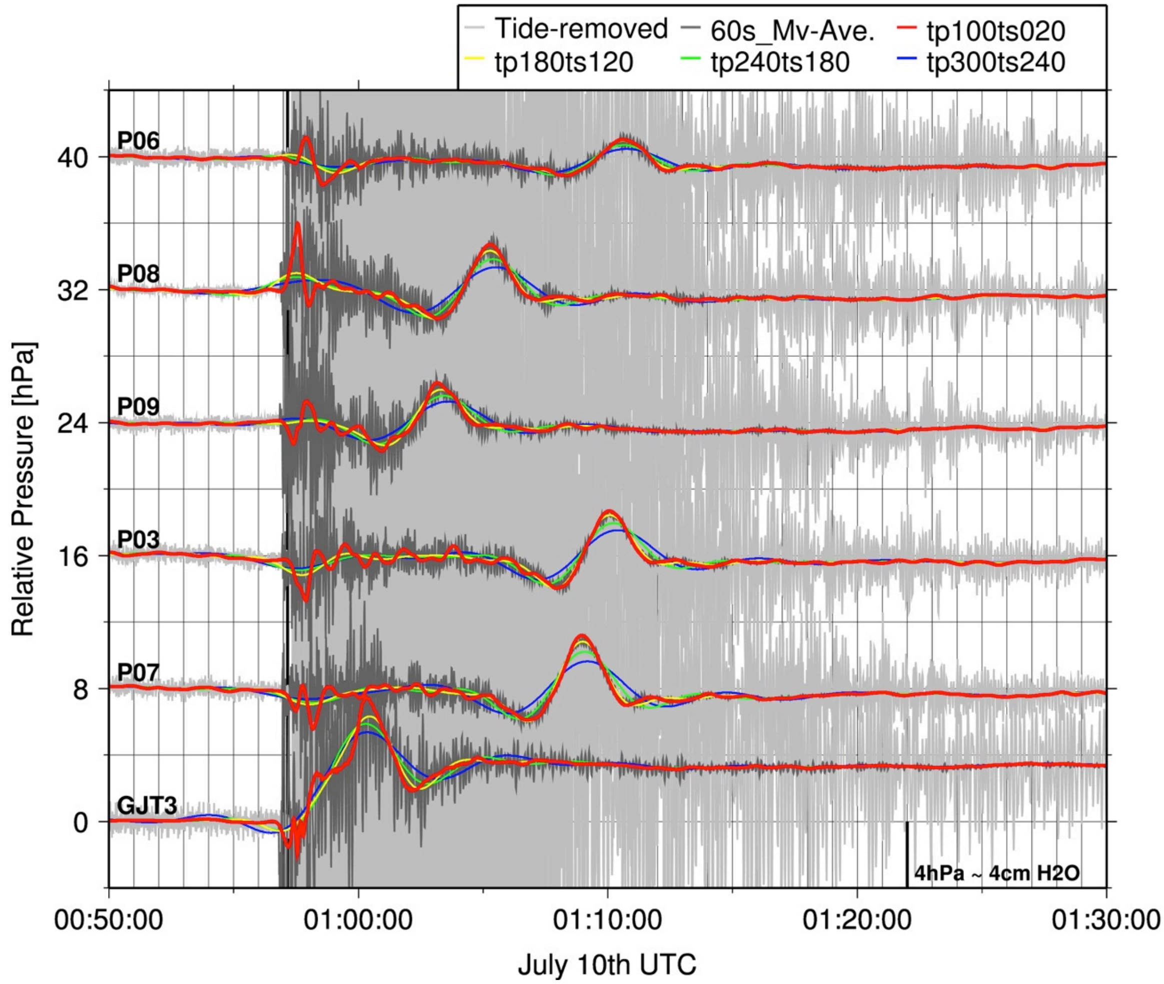

Figure S1. Comparison of low-pass filtered waveforms with several cutoff periods, de-tided waveform (light gray), and 60 s moving averaged waveform (dark gray). Cutoff parameters for the filter [Saito, 1978] were a_s = 5.0 and a_p = 0.5, and as shown in upper right legend. In the analysis, cutoff parameters of Tp = 100 s and Ts = 20 were used (red lines).

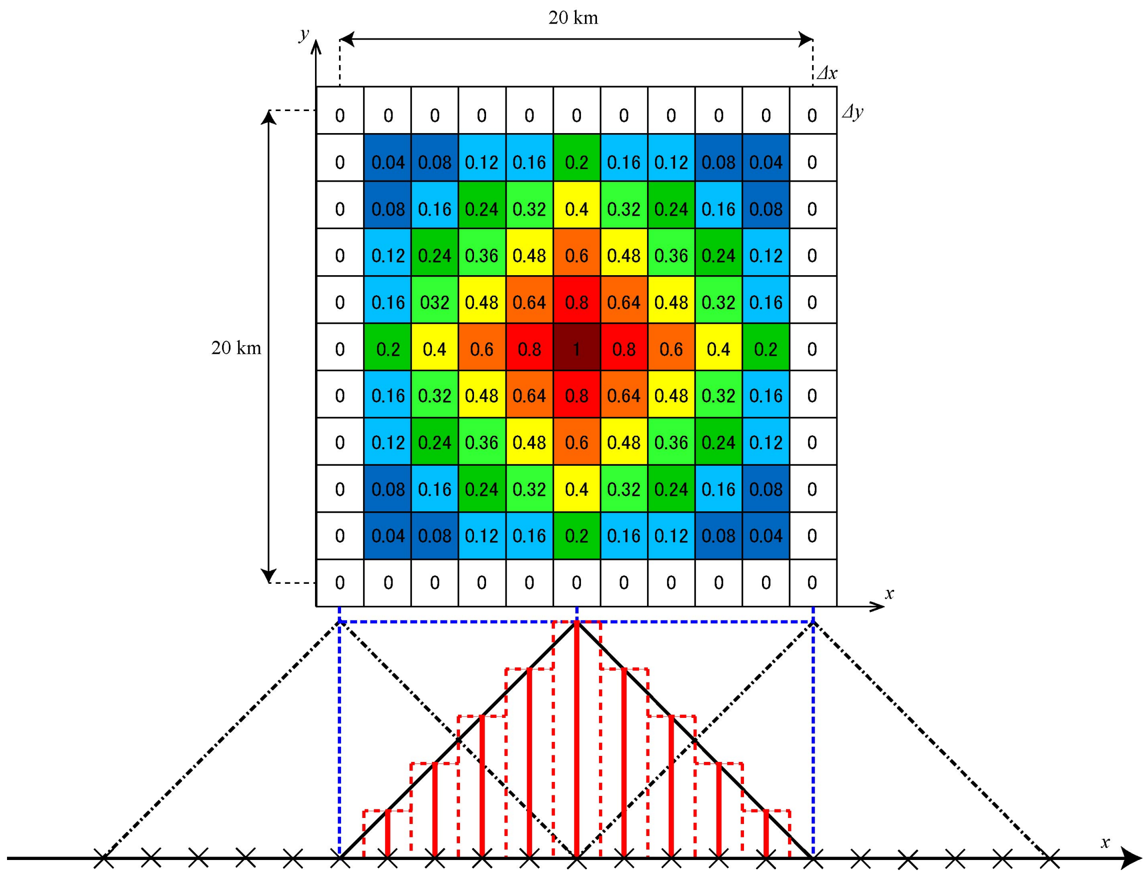

Figure S2. Schematic illustration of the unit source used in the tsunami waveform calculation. Upper figure is the top view. Each cell is enclosed by computational grids. Numerals in cells show the given amount of uplift. Lower figure is the side view. Each unit source overlaps with next ones by 10 km in length.

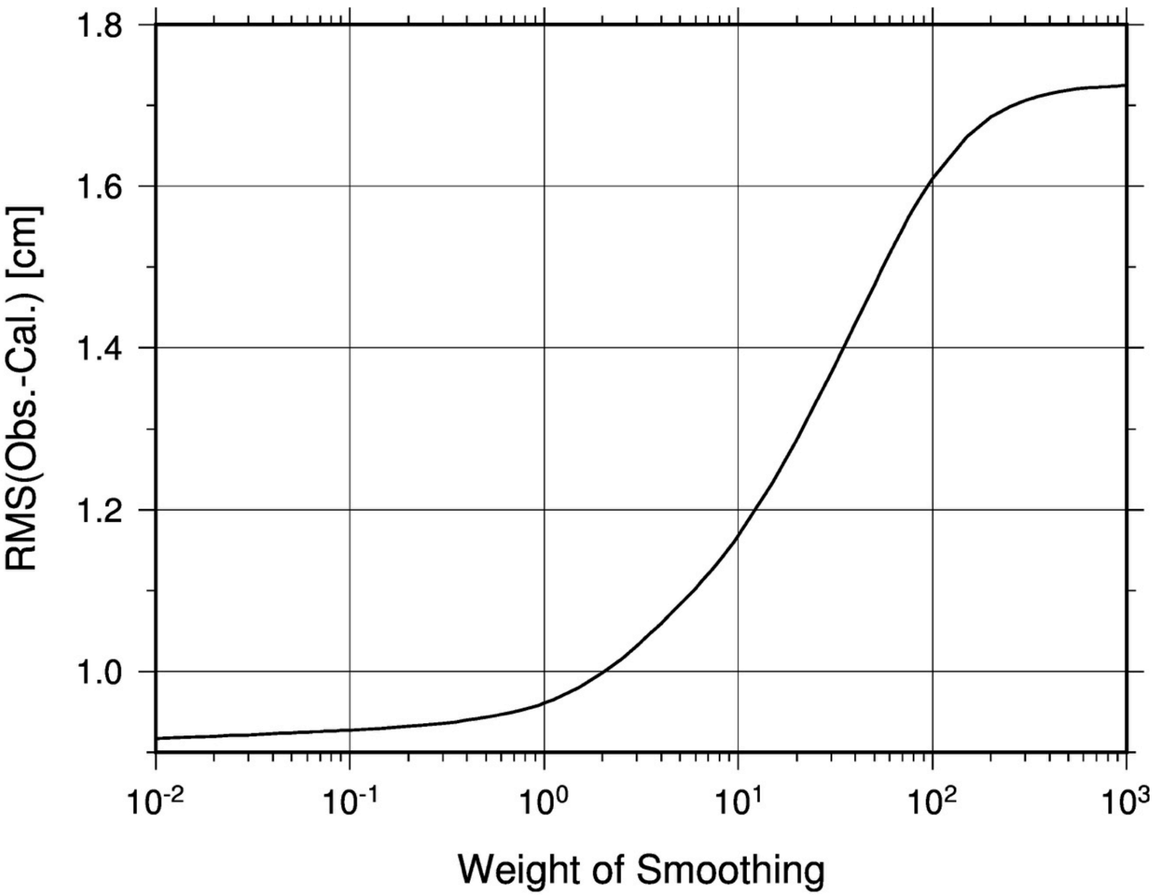

Figure S3. Trade-off curve between smoothing weight of initial sea surface height inversion and RMS misfit between observed and calculated waveforms. Because of the large curvature around 100 in the smoothing weight, we used a smoothing weight of one in the tsunami waveform inversion.

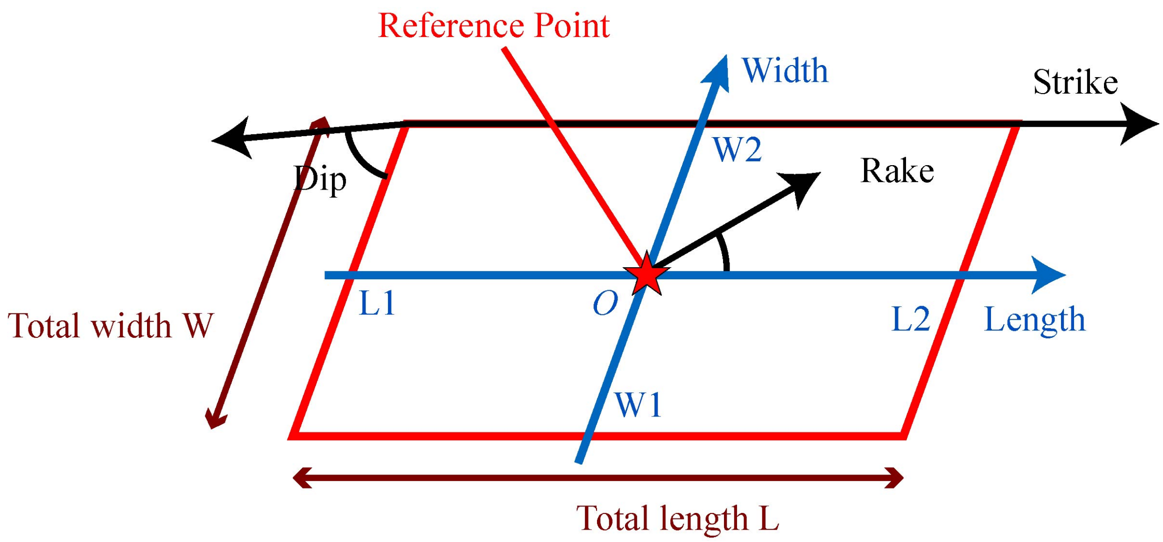

Figure S4. Schematic image of the unknown parameters in the grid-search. The origin of the fault lengths and widths (reference point) is defined as the epicenter for the fault model of 65° strike, or as the location of the CMT solution for the 330° fault model. The optimum solution is sought in the range of the parameters shown in Table S1.

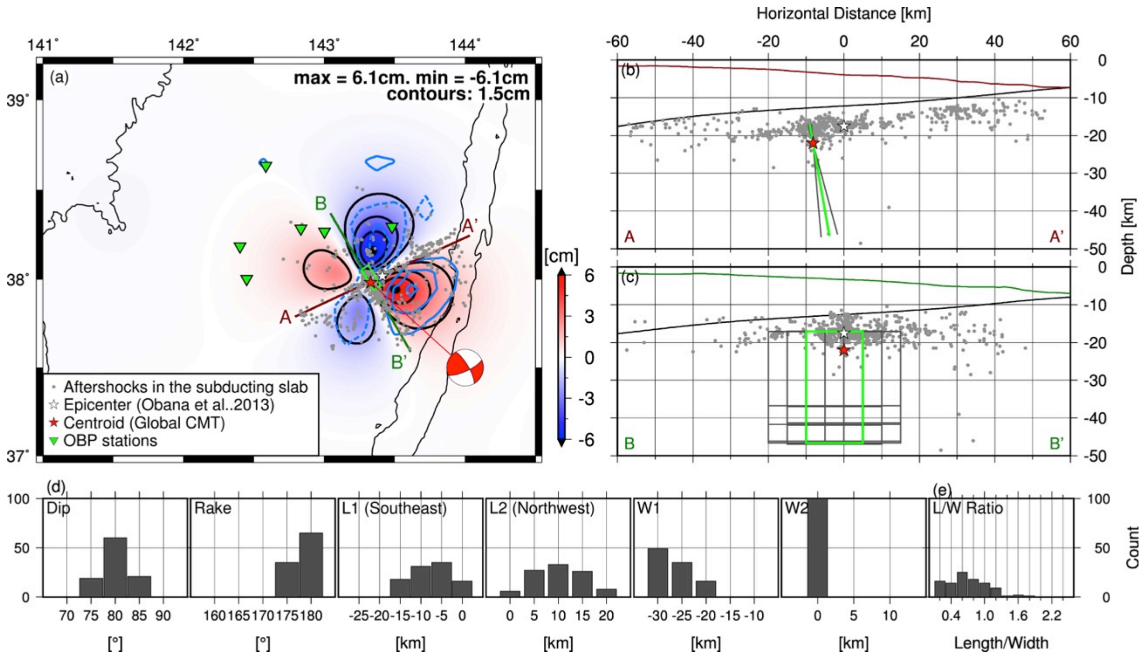

Figure S5. Result of grid search assuming fault striking NW–SE (NS model). (b) Vertical profile along A–A′ and (c) B–B′ line in Figure S4a. Red line denotes optimum fault. Black lines show top 100 solutions of grid search. Thick black curved line denotes plate boundary [*Ito et al.*, 2005]. (d) Histograms of model parameters. (e) Histogram of L/W ratios.

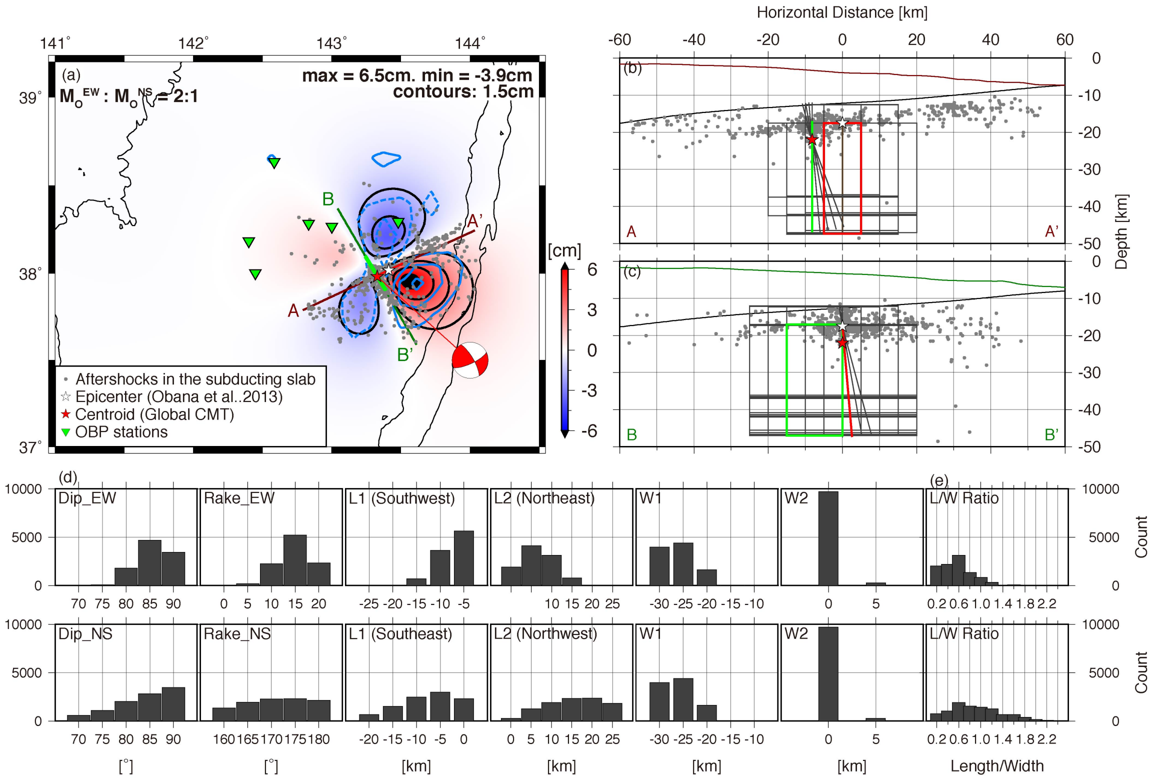

Figure S6. Result of grid search assuming uneven moment between the two faults. The best-fit model with moment ratio of 2:1 between the EW and NS faults. (a) Initial sea surface height distribution. (b) Vertical profile along A–A', and (c) B–B' lines in (a). (d) Histograms of model parameters. (e) Histogram of L/W ratios.

Table S1. Search range of the grid-search

Model	EW model	NS model	Conjugate model	
			EW fault	NS fault
Strike [°][a]	65	330	65	330
Dip [°][b]	60 – 90			
Rake [°][b]	0 – 30	150 – 180	0 – 30	150 – 180
L1 [km][c,d]	-40 – 0		-20 – 0	-25 – -10
L2 [km][c,d]	0 – 40		0 – 15	5 – 15
W1 [km][c,d,e]	-30 – -5		-30 – -5	-30 – -5
W2 [km][c,d,e]	0 – 5		0 – 5	0 – 5
Slip amount [m]	Adjusted to Mo = 3.96×10^{20} Nm with rigidity of 40 GPa.			

[a]Strike angle is fixed to the Global CMT focal mechanism.
[b]Interval of dip and rake angle parameters is 5°.
[c]Interval of parameters L1, L2, W1, and W2 is 5 km.
[d]Total fault length L and width W are defined as L2–L1 and W2–W1, respectively.
[e]The total width W and depth of the fault is constrained to be equal.